Nuclear vorticity in isoscalar $E1$ modes: Skyrme-random-phase approximation analysis

P.-G. Reinhard,[1] V. O. Nesterenko,[2] A. Repko,[3] and J. Kvasil[3]
[1]*Institut für Theoretische Physik II, Universität Erlangen, D-91058, Erlangen, Germany*
[2]*Laboratory of Theoretical Physics, Joint Institute for Nuclear Research, Dubna, Moscow region, 141980, Russia*
[3]*Institute of Particle and Nuclear Physics, Charles University, CZ-18000, Prague 8, Czech Republic*
(Received 26 December 2013; published 27 February 2014)

Two basic concepts of nuclear vorticity, hydrodynamical (HD) and Rawenthall-Wambach (RW), are critically inspected. As a test case, we consider the interplay of irrotational and vortical motion in isoscalar electric dipole $E1(T=0)$ modes in ^{208}Pb, namely the toroidal and compression modes. The modes are described in a self-consistent random-phase approximation (RPA) with the Skyrme force SLy6. They are examined in terms of strength functions, transition densities, current fields, and form factors. It is shown that the RW conception (suggesting the upper component of the nuclear current as the vorticity indicator) is not robust. The HD vorticity is not easily applicable either because the definition of a velocity field is too involved in nuclear systems. Instead, the vorticity is better characterized by the toroidal strength which closely corresponds to HD treatment and is approximately decoupled from the continuity equation.

DOI: 10.1103/PhysRevC.89.024321 PACS number(s): 24.30.Cz, 21.60.Jz, 27.80.+w

I. INTRODUCTION

It is well known that the nuclear flow may be both irrotational and vortical [1,2]. The irrotational motion is presented by numerous examples of low-energy excitations and electric giant resonances (GR) [3] while the vortical motion is exhibited by single-particle excitations [4], nuclear rotation [1], and particular GR (toroidal electric dipole [5,6] and twist magnetic quadrupole [7,8]).

Collective nuclear vorticity in electric GR is especially interesting. Though multipole electric GR are most irrotational, there is a remarkable exception in the isoscalar $E1(T=0)$ channel. Here, after exclusion of the nuclear center-of-mass (c.m.) motion, the vortical toroidal mode (TM) dominates in the low-energy ($E < 10$ MeV) $E1(T=0)$ excitations [9,10]. So, in this channel, the nuclear vorticity is realized as a leading mode. It is remarkable that the TM lies in the energy region of so-called pygmy dipole resonance (PDR) and determines there the main flow [11,12]. The low-energy strength (LES) in this region is of high current interest as it can deliver useful information on principle nuclear properties (nuclear symmetry energy, neutron skin) with consequences to various astrophysical applications [9]. The vorticity can affect these relations and thus deserves detailed analysis.

Despite some previous studies (see, e.g., [4,6,13,14]), our knowledge about the nuclear vorticity is still poor. Even the basic points, the definition of nuclear vorticity and choice of the proper observable, are disputable. In hydrodynamics (HD), the vorticity is defined as a curl of the velocity [15],

$$\vec{\varpi}(\vec{r}) = \vec{\nabla} \times \vec{v}(\vec{r}) \,. \tag{1}$$

However, nuclear physics deals not with velocities but nuclear currents. In this connection, Raventhall and Wambach have proposed the $j_+(r)$ component of the nuclear current as an indicator of the vorticity (RW vorticity in what follows) [4]. Indeed, $j_+(r)$ may be posed as unrestricted by the continuity equation (CE)

$$\delta\dot{\rho}_\nu(\vec{r}) + \vec{\nabla} \cdot \delta\vec{j}_\nu(\vec{r}) = 0 \tag{2}$$

(where $\delta\rho_\nu$ and $\delta\vec{j}_\nu$ are nucleon and current transition densities for excited states ν) and thus suitable for a divergence-free (vortical) observable [4,14,16]. However, HD and RW definitions of the vorticity strictly contradict each other [10] when being applied to the $E1(T=0)$ compression mode (CM) [17,18]. Following HD, the CM velocity field is

$$\vec{v}_{\rm CM}(\vec{r}) \propto \vec{\nabla}\,(r^3 Y_{1\mu}) \tag{3}$$

and so this mode is fully irrotational. At the same time, the CM has an essential $j_+(r)$ contribution [10] and so, following RW, is of a mixed (vortical/irrotational) character. This discrepancy certainly needs a careful analysis.

The aim of the present paper is to scrutinize the HD and RW prescriptions and finally propose the most relevant indicator and measure of the nuclear vorticity. As shown below, the RW prescription is not accurate and may result in wrong conclusions, like in the CM case mentioned above. The HD prescription (1) is more physically transparent but not convenient for practical use in nuclear physics. Instead, the toroidal strength seems to be the most appropriate (though not perfect) measure of nuclear vorticity in internal single-particle and collective excitations. Toroidal strength can be considered as an approximate HD treatment in a practicable form. It provides sufficiently good decoupling from CE (2), avoids shortcomings of the RW prescription, and exhibits a natural curl-like vortical motion.

Our analysis uses TM and CM as most relevant representatives of the vortical and irrotational flows. Schematic images of these modes in $E1(T=0)$ channel are presented in Fig. 1. Note that the TM and CM operators are related [10]. Both modes dominate the $E1(T=0)$ channel and their maxima are well separated in energy.

The calculations are performed for ^{208}Pb within the Skyrme random-phase-approximation (RPA) approach [19]. The method is fully self-consistent in the sense that both the mean field and residual interaction are derived from the Skyrme functional [20–23]. The residual interaction takes into account all the terms of the Skyrme functional as well as

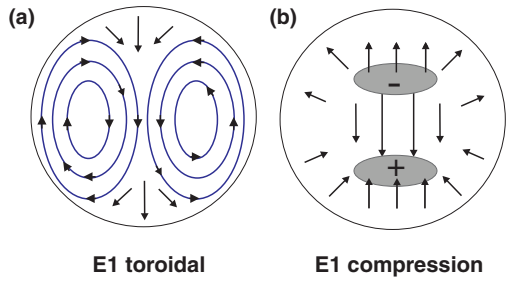

FIG. 1. (Color online) (a) Schematic view of the $E1(T=0)$ toroidal (a) and compression (b) modes [12]. The driving field is directed along the z axis. The arrows indicate the flow directions but not the strengths. In (b), the compression (+) and decompression (–) regions, characterized by increased and decreased density, are marked.

the Coulomb (direct and exchange) terms. The Skyrme force SLy6 [24], well describing the isovector ($T=1$) giant dipole resonance (GDR) in heavy nuclei [25], is used. This study is a continuation of our previous exploration of TM, CM, and RW strengths [10] within the self-consistent *separable* random-phase-approximation (SRPA) method [26,27]. The present Skyrme RPA approach does not use any separable approximation and implements a wider configuration space.

A large set of dynamical characteristics is analyzed. Not only strength functions but also current/velocity fields, and form-factors are considered. What is important, curls and divergences of TM and CM flows, as their natural signatures, are inspected. These characteristics are refined from the dominant Tassie collective modes [28] (GDR in the Goldhaber-Teller treatment [29] or spurious center of mass motion) whose velocity curls and divergences are zero [1,2,30]. At the same time, the curls and divergences are effective fingerprints of the vortical TM and irrotational CM, which are not the Tassie modes.

The paper is organized as follows. In Sec. II, the basic formalism for TM/CM modes and RW/HD vorticity prescriptions is presented. In Sec. III, the calculation scheme is outlined and the dynamical characteristics to be explored (strength functions, current/velocity fields) are defined. In Sec. IV, the numerical results are presented. In Sec. V, various prescriptions of the vorticity are discussed. The toroidal strength is shown to be the most robust measure of the vorticity. In Sec. VI, the summary is done.

II. THEORETICAL BACKGROUND

A. Basic expressions

The standard electrical multipole operator reads [31]

$$\hat{M}(E\lambda\mu,k) = -i\frac{(2\lambda+1)!!}{ck^{\lambda+1}(\lambda+1)} \times \int d^3r\, \hat{\vec{j}}_{\rm nuc}(\vec{r})\cdot[\vec{\nabla}\times(\vec{r}\times\vec{\nabla})j_\lambda(kr)Y_{\lambda\mu}(\hat{\vec{r}})] = \frac{(2\lambda+1)!!}{ck^{\lambda+1}}\sqrt{\frac{\lambda}{\lambda+1}} \times \int d^3r\,[j_\lambda(kr)\,\vec{Y}_{\lambda\lambda\mu}(\hat{\vec{r}})]\cdot[\vec{\nabla}\times\hat{\vec{j}}_{\rm nuc}(\vec{r})], \quad (4)$$

where $\hat{\vec{j}}_{\rm nuc}(\vec{r}) = \hat{\vec{j}}_{\rm c}(\vec{r}) + \hat{\vec{j}}_{\rm m}(\vec{r})$ is operator of the nuclear current density consisting from the convection and magnetization parts; $j_\lambda(kr)$ is the spherical Bessel function; $\vec{Y}_{\lambda\lambda\pm1\mu}(\hat{\vec{r}})$ and $Y_{\lambda\mu}(\hat{\vec{r}})$ are vector and ordinary spherical harmonics [33]. Following [10], the role of the magnetization current $\hat{\vec{j}}_{\rm m}(\vec{r})$ in $E1(T=0)$ channel is negligible. So only the convection current $\hat{\vec{j}}_{\rm c}(\vec{r})$ is further considered. For the sake of brevity, we will skip below (up to the cases of a possible confusion) the coordinate dependence in currents, densities and spherical harmonics.

In the long-wave approximation ($k\to 0$), we get

$$\hat{M}(E\lambda\mu,k) \approx \hat{M}(E\lambda\mu) + k\,\hat{M}_{\rm TM}(E\lambda\mu), \quad (5)$$

where

$$\hat{M}(E\lambda\mu) = -\frac{i}{kc}\int d^3r\,(\vec{\nabla}\cdot\hat{\vec{j}}_{\rm c})r^\lambda Y_{\lambda\mu} = -\int d^3r\,\hat{\rho}\,r^\lambda Y_{\lambda\mu} \quad (6)$$

is the familiar electric operator (with $\hat{\rho}$ being the density operator) and

$$\hat{M}_{\rm TM}(E\lambda\mu) = \frac{i}{2c(\lambda+1)(2\lambda+3)} \times \int d^3r\,\hat{\vec{j}}_{\rm c}\cdot[\,\vec{\nabla}\times(\vec{r}\times\vec{\nabla})r^{\lambda+2}Y_{\lambda\mu}] \quad (7)$$

$$= -\frac{1}{2c}\sqrt{\frac{\lambda}{\lambda+1}}\,\frac{1}{2\lambda+3}\int d^3r\,r^{\lambda+2}\vec{Y}_{\lambda\lambda\mu} \times(\vec{\nabla}\times\hat{\vec{j}}_{\rm c}) \quad (8)$$

is the toroidal operator [5,6,10,32]. This operator is the second order ($\sim k^2$) correction to the dominant electric operator (6). It becomes dominant at $k\gg 0$. Being determined by the curl $(\vec{\nabla}\times\hat{\vec{j}}_{\rm c})$, the toroidal flow is well (though not exactly, see discussion in Sec. IV D) decoupled from CE. For this reason the toroidal operator cannot be presented through the nuclear density alone and needs knowledge of the current distribution.

The CM operator reads [10,17,18]

$$\hat{M}_{\rm CM}(E\lambda\mu) = -\frac{i}{2c(2\lambda+3)}\int d^3r\,r^{\lambda+2}Y_{\lambda\mu}(\vec{\nabla}\cdot\hat{\vec{j}}_{\rm c}) \quad (9)$$

$$= -k\frac{1}{2(2\lambda+3)}\int d^3r\hat{\rho}r^{\lambda+2}Y_{\lambda\mu} \quad (10)$$

$$= -k\hat{M}'_{\rm CM}(E\lambda\mu), \quad (11)$$

where $\hat{M}'_{\rm CM}(E\lambda\mu)$ is its familiar density-dependent form [17,18]. The CM operator does not follow from the long-wave expansion of the initial electric operator (4) but is introduced as a proper probe operator for excitation of the isoscalar dipole giant resonance [17,18]. Unlike the TM case, this operator may be presented in both current- and density-dependent forms. As mentioned above, the velocity of the CM flow is a gradient function, which justifies the irrotational (longitudinal) character of the flow.

As was found in [10], the sum of the TM and CM operators gives the operator responsible for RW vorticity:

$$\hat{M}_{\rm RW}(E\lambda\mu) = \hat{M}_{\rm TM}(E\lambda\mu) + \hat{M}_{\rm CM}(E\lambda\mu)\ . \qquad (12)$$

This relation makes possible a direct comparison of RW, TM, and CM strengths. Besides, it shows that all these three operators are of the second order with respect to the electric operator (6).

B. $E1(T = 0)$ case

In the $E1(T = 0)$ channel, the RW, TM, and CM operators are reduced to

$$\hat{M}_{\rm RW}(E1\mu) = -\frac{i}{5c}\sqrt{\frac{3}{2}}\int d^3r\,\hat{\vec{j}}_c r^2 \vec{Y}_{12\mu}, \qquad (13)$$

$$\hat{M}_{\rm TM}(E1\mu) = -\frac{i}{2\sqrt{3}c}\int d^3r\,\hat{\vec{j}}_c \times\left[\frac{\sqrt{2}}{5}r^2\vec{Y}_{12\mu} + (r^2 - \langle r^2\rangle_0)\vec{Y}_{10\mu}\right], \qquad (14)$$

$$\hat{M}_{\rm CM}(E1\mu) = -\frac{i}{2\sqrt{3}c}\int d^3r\,\hat{\vec{j}}_c \times\left[\frac{2\sqrt{2}}{5}r^2\vec{Y}_{12\mu} - (r^2 - \langle r^2\rangle_0)\vec{Y}_{10\mu}\right], \qquad (15)$$

$$\hat{M}'_{\rm CM}(E1\mu) = \frac{1}{10}\int d^3r\hat{\rho}\,\left[r^3 - \frac{5}{3}\langle r^2\rangle_0 r\right]Y_{1\mu}. \qquad (16)$$

Here, $\langle r^2\rangle_0 = \int d^3r\rho_0 r^2/A$ is the ground-state squared radius, $\rho_0(\vec{r})$ is the ground state density, A is the mass number. The operators (14)–(16) have the center-of-mass correction (c.m.c.) proportional to $\langle r^2\rangle_0$, while in Eq. (13) the c.m.c. is zero. In what follows, we consider only $\mu = 0$ case and thus skip the μ index.

The RW, TM, and CM matrix elements for $E1$ transitions between the ground state $|0\rangle$ and RPA excited state $|\nu\rangle$ can be determined through the current transition density

$$\delta\vec{j}^{\nu}(\vec{r}) = \langle\nu|\,\hat{\vec{j}}_c(\vec{r})\,|0\rangle = \left[j^{\nu}_{10}(r)\,\vec{Y}^*_{10} + j^{\nu}_{12}(r)\,\vec{Y}^*_{12}\right] \qquad (17)$$

as

$$\langle\nu|\hat{M}_{\rm RW}(E1)|0\rangle = -\frac{1}{5\sqrt{2}c}\int dr r^4 j^{\nu}_{12}, \qquad (18)$$

$$\langle\nu|\hat{M}_{\rm TM}(E1)|0\rangle = -\frac{1}{6c}\int dr r^2 \times\left[\frac{\sqrt{2}}{5}r^2 j^{\nu}_{12} + (r^2 - \langle r^2\rangle_0)j^{\nu}_{10}\right], \qquad (19)$$

$$\langle\nu|\hat{M}_{\rm CM}(E1)|0\rangle = -\frac{1}{6c}\int dr r^2 \times\left[\frac{2\sqrt{2}}{5}r^2 j^{\nu}_{12} - (r^2 - \langle r^2\rangle_0)j^{\nu}_{10}\right]. \qquad (20)$$

The upper and lower current components are usually denoted as j_+ and j_- ($j_+ = j_{12}$ and $j_- = j_{10}$ in the $E1$ case). In accordance to [4], just j_+ determines the vorticity [and RW matrix element (18)]. The flow can be fully vortical ($j_+ \neq 0$, $j_- = 0$), fully irrotational ($j_+ = 0$, $j_- \neq 0$), and mixed ($j_+ \neq 0$, $j_- \neq 0$). Following this prescription, both TM and CM are of a mixed (irrotational/vortical) character, which contradicts with predominantly curl- and gradient-like velocities of these flows [10].

C. Hydrodynamical vorticity

To analyze the HD vorticity (1), we should define the velocity of a nuclear motion and build the corresponding matrix elements. This can be done by definition of the velocity transition density through the current one [13],

$$\delta\vec{v}^{\nu}(\vec{r}) = \frac{\delta\vec{j}^{\nu}(\vec{r})}{\rho_0(\vec{r})}\ , \qquad (21)$$

and the replacement

$$[\vec{\nabla}\times\delta\vec{j}^{\nu}(\vec{r})] \to \rho_0(\vec{r})[\vec{\nabla}\times\delta\vec{v}^{\nu}(\vec{r})] \qquad (22)$$

in the relevant matrix elements. It is easy to see from the exact expression

$$\vec{\nabla}\times\delta\vec{j}^{\nu}(\vec{r}) = \rho_0(\vec{r})\vec{\nabla}\times\delta\vec{v}^{\nu}(\vec{r}) + \vec{\nabla}\rho_0(\vec{r})\times\delta\vec{v}^{\nu}(\vec{r}) \qquad (23)$$

that the replacement (22) neglects $\vec{\nabla}\rho_0(\vec{r})$ and thus a large change of $\rho_0(\vec{r})$ at the nuclear surface. So, the HD vorticity build from Eq. (22) is relevant by construction only at nuclear interior.

Among RW, TM, and CM operators, only the TM one (8) and its matrix element

$$\langle\nu|\hat{M}_{\rm TM}(E1)|0\rangle = -\frac{1}{10\sqrt{2}c}\int d^3r\left[r^3 - \frac{5}{3}r\langle r^2\rangle_0\right]\vec{Y}_{11}\cdot[\vec{\nabla}\times\delta\hat{\vec{j}}^{\nu}] \qquad (24)$$

have the necessary curl-of-current structure suitable for using the replacement (22). Then, by substituting Eq. (22) into Eq. (24), we get the matrix element

$$\langle\nu|\hat{M}_{\rm HD}(E1)|0\rangle = -\frac{1}{10\sqrt{2}c}\int d^3r\left[r^3 - \frac{5}{3}r\langle r^2\rangle_0\right]\rho_0\vec{Y}_{11}\cdot[\vec{\nabla}\times\delta\hat{\vec{v}}^{\nu}], \qquad (25)$$

characterizing the HD vorticity. The explicit expressions for curls and divergences of $\delta\hat{\vec{j}}^{\nu}$ and $\delta\hat{\vec{v}}^{\nu}$ are given in Appendix A.

Note that, though the general electric operator (4) also has the curl-of-current term, it cannot be used for building HD matrix elements through the replacement (22). Indeed the vorticity is the second-order divergence-free effect vanishing in the long-wave ($k \to 0$) approximation (LWA). Instead, the operator (4) still has the LWA contribution.

Definition of the velocity (21) has a well-known shortcoming. Being inverse to the density $\rho_0(\vec{r})$, the velocity becomes artificially large at the nuclear surface and beyond. This shortcoming persists in the HD matrix elements (25). As was mentioned above in connection to Eq. (23), the HD vorticity built from Eq. (22) may be applied only to the nuclear interior where $\rho_0(\vec{r})$ changes smoothly. The toroidal flow is similar to HD in the interior but has a good behavior at the surface. Thus the TM strength is a more robust measure of the HD vorticity than the construction (25). This will be confirmed in Sec. IV by numerical results.

III. METHOD

For analysis of the nuclear vorticity, a representative set of variables is used: strength functions, flow patterns and coordinate-energy maps for current (velocity) transition densities and their derivatives (curls and divergences), and form factors.

A. Strength function

The energy distribution of the mode strengths is described by the strength function

$$S_\alpha(E1;\omega) = 3\sum_\nu \omega_\nu^l |\langle\nu|\hat{M}_\alpha(E1)|0\rangle|^2 \zeta(\omega-\omega_\nu) \qquad (26)$$

involving the Lorentz weight

$$\zeta(\omega-\omega_\nu) = \frac{1}{2\pi}\frac{\Delta}{(\omega-\omega_\nu)^2+\frac{\Delta^2}{4}} \qquad (27)$$

with the smoothing width Δ. The type of the transition operator $\hat{M}_\alpha(E1)$ is determined by the index $\alpha = \{E1,\text{RW, TM, CM, HD}\}$, ν runs over the RPA spectrum with eigenfrequencies ω_ν and eigenstates $|\nu\rangle$. The $E1(T=1)$ strength function ($\alpha = E1$) uses the energy weight ($l=1$) and the ordinary $E1$ operator with the effective charges $e^n_{\text{eff}} = -Z/A$ and $e^p_{\text{eff}} = N/A$ (see the operator $\hat{D}_1$ below). Other strength functions with $\alpha = \{\text{RW, TM, CM, HD}\}$ skip the energy weight ($l=0$) and, being studied in $T=0$ channel, use $e^n_{\text{eff}} = e^p_{\text{eff}} = 1$.

B. Flow patterns and coordinate-energy maps

The strength functions provide a first overview of the modes. A more insight can be gained by inspection of the current (velocity) transition densities and their derivatives.

Since we are interested in general features of the modes, it is convenient to consider the *integral* variables (involving contributions from all the RPA states in a given energy interval $[E_1,E_2]$)

$$\vec{A}^{(D)}(\vec{r}) = \sum_{\nu\epsilon[E_1,E_2]} D^*_\nu \vec{A}^\nu(\vec{r}), \qquad (28)$$

$$B^{(D)}(\vec{r}) = \sum_{\nu\epsilon[E_1,E_2]} D^*_\nu B^\nu(\vec{r}), \qquad (29)$$

or *average* variables (smoothed by the Lorentz weight ζ)

$$C^{(D)}(r,\omega) = \sum_\nu D^*_\nu C^\nu(r)\zeta(\omega-\omega_\nu)\,. \qquad (30)$$

The vectors variables $\vec{A}^{(D)}(\vec{r})$ give the flow patterns describing in detail the coordinate (radial and angular) distribution of the modes. The vector contributions $\vec{A}^\nu(\vec{r})$ could be the current/velocity transition densities, their components and curls. Further, the variables $B^{(D)}(\vec{r})$ provide the similar coordinate distribution but for the scalar patterns like divergences of the flows. The coordinate-energy maps $C^{(D)}(r,\omega)$ deliver information on radial/energy distribution, thus combining properties of the transition densities and strength functions. Using Eqs. (28)–(30) allows to avoid individual details of RPA states but highlight their common features.

The calculation of such variables needs a precaution because of arbitrary signs of RPA ν states. To overcome this trouble, we use the technique [12] where the values of interest are additionally weighted by the matrix elements $D_\nu = \langle\nu|\hat{D}_T(E1)|0\rangle$ of the dipole probe operator $\hat{D}_T(E1)$. Then every state ν contributes to Eqs. (28)–(30) twice and thus the ambiguity is removed. Two dipole probe operators are implemented: isovector

$$\hat{D}_1(E1) = (N/A)\sum_i^Z (rY_1)_i - (Z/A)\sum_i^N (rY_1)_i \qquad (31)$$

for the GDR (giant dipole resonance, $\alpha = E1$) strength and isoscalar

$$\hat{D}_0(E1) = \sum_i^A (r^3Y_1)_i \qquad (32)$$

for the modes $\alpha = \{\text{RW, TM, CM, HD}\}$.

For example, for the current transition density $\delta\vec{j}(\vec{r})$ and its radial component $j_{21}(r)$, the variables (28) and (30) read

$$\delta\vec{j}_1^{(D_0)}(\vec{r}) = \sum_{\nu\epsilon[E_1,E_2]} D^*_\nu \delta\vec{j}_1^\nu(\vec{r}), \qquad (33)$$

$$\delta j_{12}^{(D_0)}(r,\omega) = \sum_\nu D^*_\nu \delta j^\nu_{12}(r)\zeta(\omega-\omega_\nu). \qquad (34)$$

The explicit expressions for other cases are given in Appendix B.

C. Form factors

The form factors are obtained from the average variables (30) by the Fourier-Bessel transformation

$$F^{(D)}(k,\omega) = \sum_\nu D^*_\nu \zeta(\omega-\omega_\nu)\int drr^2 j_1(kr)C^\nu(r), \qquad (35)$$

where $j_1(r)$ is the dipole spherical Bessel function.

D. Calculation details

The calculations are performed within the one-dimensional (1D) Skyrme RPA approach [19,23]. The approach is fully self-consistent in the sense that both the mean field and residual interaction are derived from the Skyrme functional [20–23]. Besides, the residual interaction takes into account all terms of the Skyrme functional as well as the Coulomb (direct and exchange) terms. There is no variational c.m.c. term in the functional. The calculations are performed for the doubly magic nucleus ^{208}Pb. We use the Skyrme force SLy6 [24] providing a good description of the GDR in heavy nuclei [25].

The calculations employ a 1D spherical coordinate-space grid with the mesh size 0.3 fm and a calculational box of 21 fm. We have tested smaller spacings down to 0.1 fm and find no visible difference in the RPA spectra. So the present grid provides quite accurate results for averaged characteristics (26)–(30) and (35) considered in the present study. A large RPA expansion basis is used. The particle-hole (1ph) states are included up to an excitation energy of ∼35 MeV. Furthermore, we employ a couple of fluid dynamical basis modes [19], which

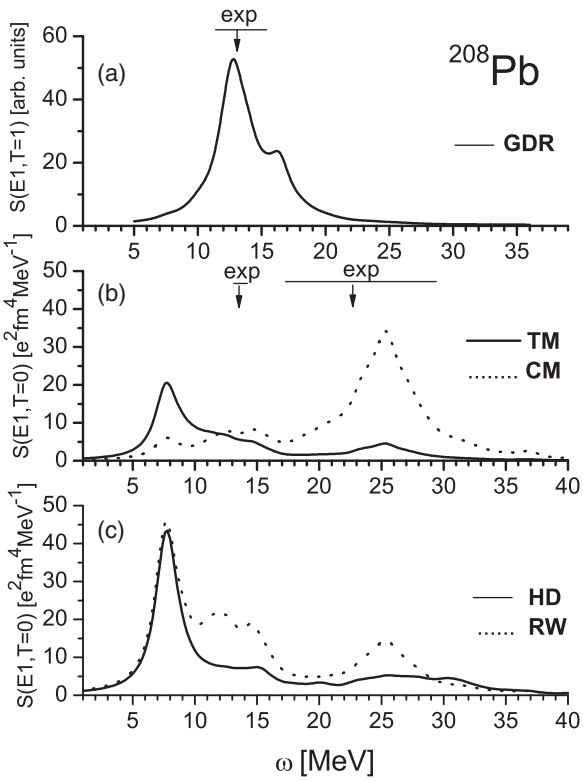

FIG. 2. The RPA strength functions. (a) $E1(T = 1)$ GDR. The line with the arrow indicate the experimental width and energy centroid of the resonance [34]. (b) $E1(T = 0)$ toroidal (TM, solid line) and compression (CM, dotted line) strengths. The widths and energy centroids of the low- and high-energy branches of $E1(T = 0)$ excitations observed in (α,α') reaction [35,36] are denoted. (c) The $E1(T = 0)$ hydrodynamical (HD, solid line) and Rawenthal-Wambach (RW, dotted line) vortical strengths.

allows to: i) include global polarization effects up to 200 MeV, ii) provide correct extraction of the center-of-mass mode, and iii) produce 100% exhaustion of the energy-weighted sum rules for the isovector [2] and isoscalar [3] GDR.

The strength functions (26), coordinate-energy maps (30), and form factors (35) employ the Lorentz weight (27) with the constant smoothing width $\Delta = 1$ MeV. This smoothing allows to avoid unnecessary details and provide a reasonable averaging.

IV. NUMERICAL RESULTS

A. Strength functions

In Fig. 2, the relevant RPA strength functions in ^{208}Pb are exhibited. [Note that plots (a,b) of this figure somewhat deviate from the similar plots in our previous study of the pygmy resonance [12]. This is caused by using in [12] the energy-dependent smoothing width $\Delta(\omega)$].

In Fig. 2(a), the calculated isovector GDR is compared to the experimental data [34]. A good agreement with the experiment justifies a satisfactory accuracy of our description.

Further, panels (b), (c) demonstrate the TM, CM, HD, and RW strengths in the $E1(T = 0)$ channel. Note that due to the large configuration space and c.m.c. in the transition matrix elements (19), (20), and (25), the spurious strength is fully downshifted below 0.5 MeV and thus does not affect the results. Panel (b) shows that the calculated TM and CM strengths are peaked at 7–8 MeV and ∼25 MeV, respectively. These results somewhat deviate from available experimental (α,α') data for the $E1(T = 0)$ resonance [35,36] which give maxima at 12.7 and 23.0 MeV. Such discrepancy is common for various theoretical approaches [9] and worth to be commented in more detail.

First of all, following panel (b), the measured $E1(T = 0)$ resonance may be treated as manifestation of the CM alone, i.e., without TM contribution. Indeed, the experimental peaks at 12.7 and 23.0 MeV can correspond to the CM structures at 13–15 and 25 MeV in our RPA calculations. The familiar interpretation of the experimental peak at 12.7 MeV as TM [35,36] is questionable since the calculated TM lies much lower, namely at 7–8 MeV. The experiment [35,36] explores the excitation energy interval 8–35 MeV and perhaps loses the strong and narrow TM peak at 7–8 MeV. Moreover, the (α,α') reaction, being mainly peripheral, is generally not suitable for observation of the vortical TM.

Further, the discrepancy for CM energy (25 MeV in the theory versus 23 MeV in the experiment) may be explained by a sensitivity of this high-energy strength to the calculation scheme, in particular to the size of the configuration space. The larger the space, the lower the CM energy. It seems that even our impressive space size (up to ∼200 MeV) is not yet enough. Perhaps, the coupling to complex configurations has here some effect.

Our RPA results are close to the previous relativistic [37,38] and Skyrme nonrelativistic [10,39] studies, including SRPA ones [10]. Note that the TM lies at 6–9 MeV, i.e., at the PDR location. Following [12], the $E1(T = 0)$ strength in this region has a complex composition with a strong toroidal fraction.

Panel (c) exhibits the RW and HD strengths calculated with the transition dipole matrix elements (18) and (25), respectively. As mentioned above, both them were proposed as the vortical fingerprints. It is seen that RW and HD give about equal strong peaks at 7–8 MeV, i.e., just at the TM energy. So both them signal on the truly TM vortical motion. However, the RW and HD deviate at higher energies. The HD, being similar to TM by construction, is modest everywhere with exception of the TM region. Instead, the RW has additional maxima at the GDR (10–15 MeV) and CM (25 MeV) regions, characterized by strong irrotational flows. This means that RW is not a robust measure of the vorticity.

In Fig. 3, the contributions of $j_-(r) \equiv j_{10}(r)$ and $j_+(r) \equiv j_{12}(r)$ components of the nuclear current (17) to $E1(T = 0)$ TM, CM, RW, and HD strengths are demonstrated. It is seen that both components are peaked in low-energy (LE) and high-energy (HE) regions, with some preference of LE for j_+ and HE for j_-. Following expressions (19), (20), (25), and Appendix A, the TM, CM, and HD strengths are produced by constructive or destructive interference of j_+ and j_- (or v_+ and v_-) contributions. The LE interference is constructive for TD/HD and destructive for CM. For HE, the picture is opposite. The RW is by construction fully determined by j_+. Following Fig. 3, there is no any essential advantage of j_+

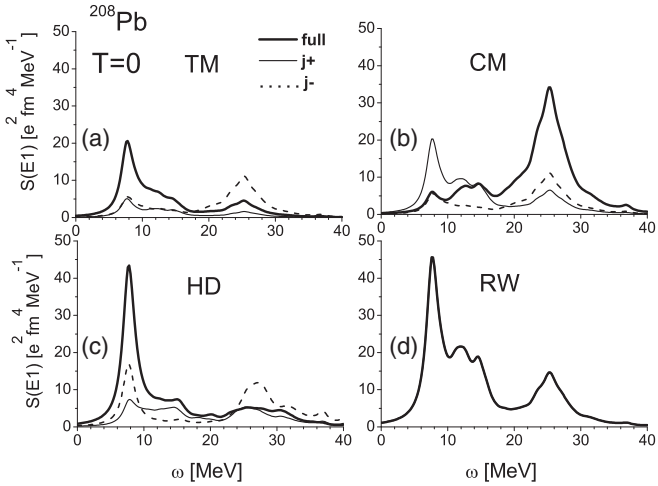

FIG. 3. (a) Toroidal (TM), (b) compression (CM), (c) hydrodynamical (HD), and (d) Rawenthal-Wambach (RW) RPA strength functions for the full nuclear current (bold line) and its $j_- \equiv j_{10}$ (dotted line) and $j_+ \equiv j_{12}$ (thin line) components. For RW case, we have $j_- = 0$ and so only $j = j_+$ strength is shown.

over j_- to represent the nuclear vorticity. Both components are almost equally active in the vortical TM at 7–8 MeV and irrotational CM at 25 MeV. This once more distrusts j_+ as a vortical descriptor.

B. Flow patterns

As compared to the strength functions, the flow patterns deliver a more detailed information on nuclear dynamics. Here we depict not only nuclear current and velocity fields but also their divergences and curls. The patterns $\vec{\nabla}\cdot\vec{j}$ and $\vec{\nabla}\times\vec{j}$ are especially important since they directly indicate if the current contributes to CE. Obviously, only curl-free ($\vec{\nabla}\times\vec{j}=0$) currents are irrotational and coupled to CE. Instead, the divergence-free ($\vec{\nabla}\cdot\vec{j}=0$) currents carry the vorticity and are CE unrestricted.

Note that the isovector GDR (in the Goldhaber-Teller model [29]) and isoscalar spurious c.m. motion are basically driven by the operator $rY_{1\mu}$ with the velocity field $\vec{v}\propto\vec{\nabla}(rY_{1\mu})$. They are collective Tassie modes with $\vec{\nabla}\cdot\vec{v}=\vec{\nabla}\times\vec{v}=0$ [1,2,28,30] and thus their contributions to $\vec{\nabla}\cdot\vec{j}$ and $\vec{\nabla}\times\vec{j}$ is strongly suppressed, at least at the nuclear interior. Instead, the $E1$ TM and CM are characterized by the operators with r^3 dependence and so do not belong the Tassie modes. For them, the patterns $\vec{\nabla}\cdot\vec{j}$ and $\vec{\nabla}\times\vec{j}$ are indeed instructive.

In Fig. 4, different patterns for the energy bin 6–9 MeV containing the TM are considered. Panel (a) shows that, in accordance with our previous study [12], the current $\vec{j}$ is mainly of the toroidal nature [to be compared to Fig. 1(a) for the schematic image of TM]. The same takes place for the velocity field $\vec{v}$ exhibited in panel (b). The velocity is not damped by the density factor and so is artificially strong at the nuclear surface (marked by the circle of the radius $R=1.16$ fm $A^{-1/3}$) and beyond. Following panels (c) and (e), the current curl is much stronger than its divergence, which

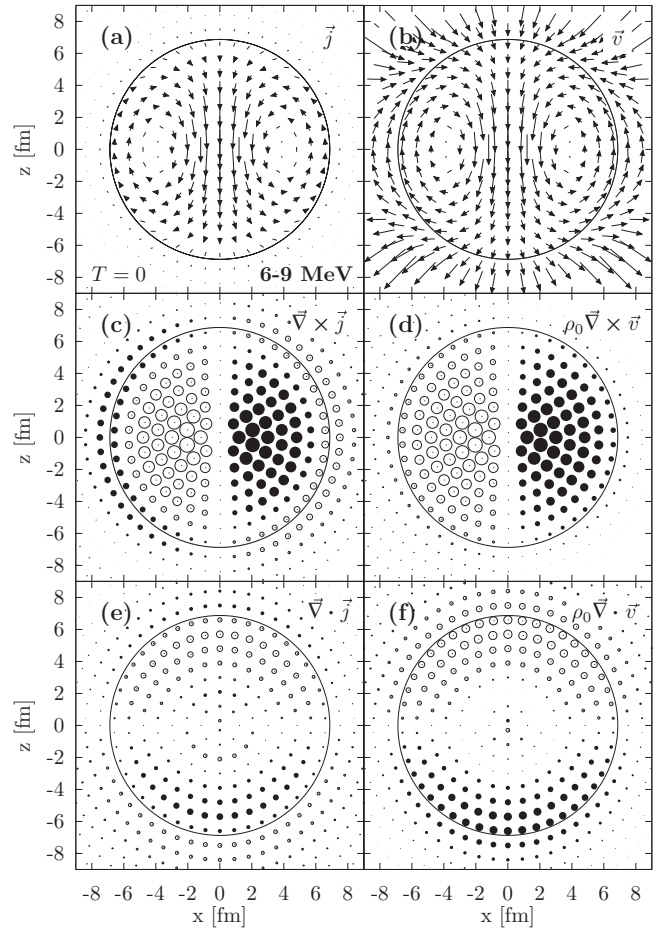

FIG. 4. $E1(T=0)$ current and velocity flow patterns (28) and (29) at the x-z plane for the TM energy bin 6–9 MeV in ^{208}Pb: (a) nuclear current $\vec{j}$, (b) nuclear velocity $\vec{v}$, (c) current curl $\vec{\nabla}\times\vec{j}$, (d) velocity curl $\rho_0\vec{\nabla}\times\vec{v}$, (e) current divergence $\vec{\nabla}\cdot\vec{j}$, and (f) velocity divergence $\rho_0\vec{\nabla}\cdot\vec{v}$. In (c) and (d), the flows, being perpendicular to the plane x-z, are exhibited by circles. The open (filled) circles represent flows along (opposite to) the y axis. In (e) and (f), the open (filled) circles represent positive (negative) values. The flow magnitude is depicted by the size of the arrows and circles (in arbitrary units). The nuclear boarder is marked by a large circle. See explicit expressions for patterns in Appendix B.

confirms basically vortical character of the flow. The density-weighted curl and divergence of the velocity in panels (d)–(f) are very similar to their current counterparts in the nuclear interior. A difference takes place only at the nuclear surface. So, up to the surface region, the HD vorticity determined by $\vec{\nabla}\times\vec{v}$ can be well characterized by $\vec{\nabla}\times\vec{j}$.

As shown in Sec. II, the TM and CM operators are composed from $\vec{j}_+$ and $\vec{j}_-$ components of the nuclear current. Moreover, following [4], the component $\vec{j}_+$ is treated as a measure of the nuclear vorticity. So it is worth to inspect the $\vec{j}_+$ and $\vec{j}_-$ flows in more detail. The relevant flow patterns are given in Fig. 5. Panels (a) and (b) show that $\vec{j}_+$ and $\vec{j}_-$ are essentially different: the former is maximal in the north and south poles while the later is maximal in the nuclear center. Despite this difference, curls of $\vec{j}_+$ and $\vec{j}_-$ are rather

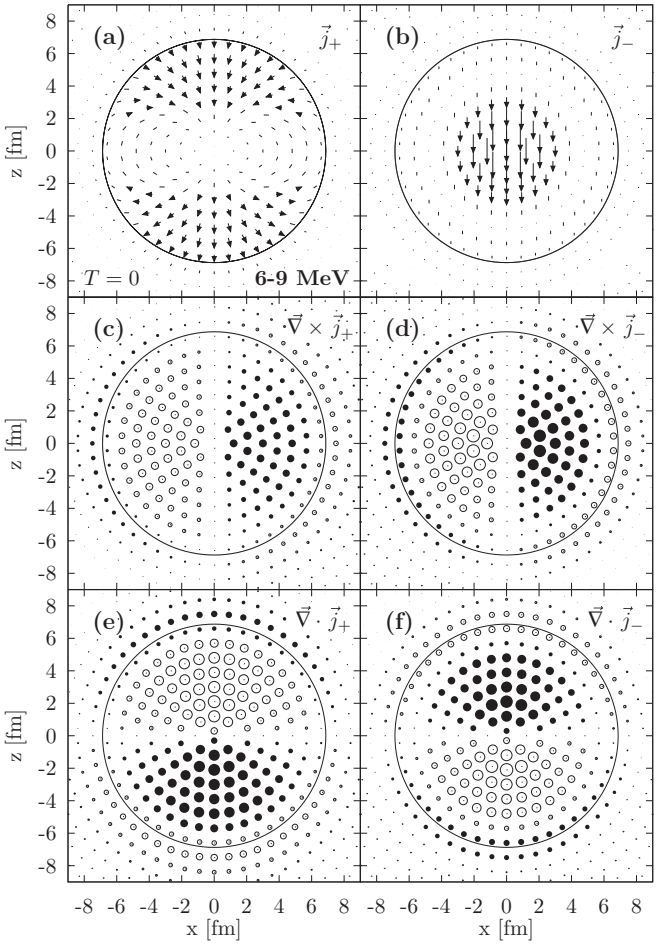

FIG. 5. $E1(T = 0)$ flow patterns for the current components $\vec{j}_+$ (left) and $\vec{j}_-$ (right) at the x-z plane for the TM energy bin 6–9 MeV in ^{208}Pb. The current components $\vec{j}_\pm$ (a) and (b), as well as their curls (c) and (d) and divergences (e) and (f) are exhibited. The presentation is similar to that in Fig. 4. See explicit expressions for the patterns in Appendix B.

similar [panels (c) and (d)]. The same takes place (up to the total sign) for the divergencies [panels (e) and (f)]. Moreover, divergences and curls of $\vec{j}_+$ and $\vec{j}_-$ are of the same order of magnitude. So none of these current components alone is suitable to represent neither vortical nor irrotational flows. Only their proper combinations, like TM and CM ones, may be appropriate for this aim. The value $\vec{j}_+$ has no any significant advantage over $\vec{j}_-$ as a measure of the vorticity, which makes the RW vorticity criterium [4] questionable.

In Fig. 6, both $\vec{j}$ and $\vec{v}$ reproduce the typical compression dipole motion [to be compared to Fig 1(b) for the schematic image of CM]. The divergence of the current is stronger than its curl. This is natural for CM which, being almost irrotational, is not however the Tassie divergence-free mode.

C. Coordinate-energy maps and form-factors

In Fig. 7, the smoothed coordinate-energy maps (30) for divergence and curl of the nuclear current are given for 1ph (unperturbed Hartree-Fock) and RPA $E1(T = 0)$ excitations.

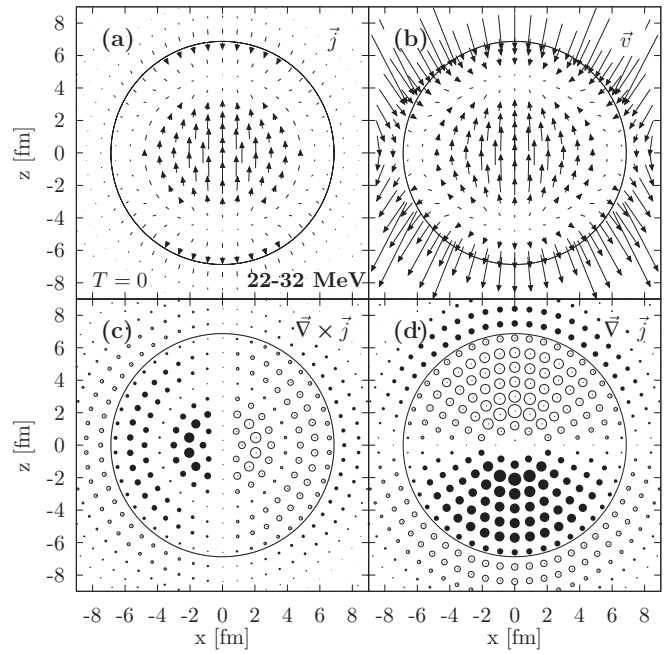

FIG. 6. $E1(T = 0)$ flow patterns in ^{208}Pb for the CM energy bin 22–32 MeV. See Fig. 4 for notation.

It is seen that both $\vec{\nabla} \cdot \vec{j}$ and $\vec{\nabla} \times \vec{j}$ are strong in a wide radial region 3 fm $< r <$ 10 fm around the nuclear surface at $\sim$7 fm. Following panels (a), (b), the 1ph strength is concentrated in broad energy intervals: low-energy (LE) 4–17 MeV and high-energy (HE) 28–35 MeV. In both intervals, the curl and divergence are strong. The strength is multimodal, which is common for noncollective (single-particle) excitations.

As seen from panels (c) and (d) for the RPA case, inclusion of the residual interaction considerably changes the pictures.

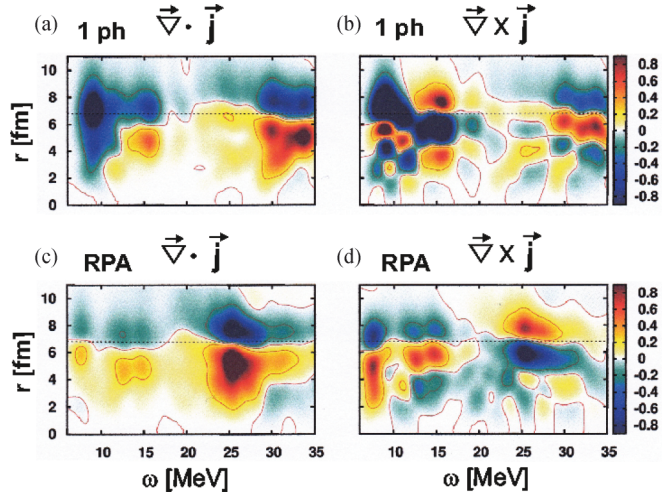

FIG. 7. (Color online) The coordinate-energy maps for the divergence (a), (c) and curl (b), (d) of the nuclear current in the $E1(T = 0)$ channel in ^{208}Pb. The upper (a), (b) and lower (c), (d) panels represent the 1ph and RPA strengths, respectively. The nuclear radius is marked by the dotted line. See explicit expressions for the patterns in Appendix B.

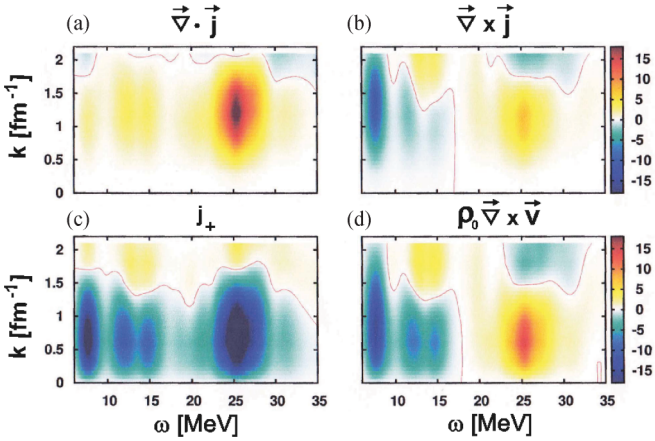

FIG. 8. (Color online) The $E1(T = 0)$ RPA formfactors in ^{208}Pb for the current divergence (a), current curl (b), j_+ component of the current (c), and density-weighted velocity curl (d). See explicit expressions for the patterns in Appendix B.

Being isoscalar, the residual interaction downshifts by energy both $\vec{\nabla} \cdot \vec{j}$ and $\vec{\nabla} \times \vec{j}$. In the CM region, the maxima are shifted from 30–35 MeV to 24–28 MeV. The RPA distributions correspond to the strength functions exhibited in Fig. 2 with the TM at ∼7 MeV, increased vorticity at 12–15 MeV and 25–30 MeV, and irrotational CM at ∼25 MeV.

Note that, after switch to RPA, both $\vec{\nabla} \cdot \vec{j}$ and $\vec{\nabla} \times \vec{j}$ become weaker in the GDR region 10-15 MeV. For the first glance, this result looks surprising. However both isovector GDR and isoscalar spurious c.m. motion are basically the collective Tassie modes with suppressed $\vec{\nabla} \cdot \vec{j}$ and $\vec{\nabla} \times \vec{j}$. Then panels (c) and (d) actually show the rest of $\vec{\nabla} \cdot \vec{j}$ and $\vec{\nabla} \times \vec{j}$ not yet washed out by the dominant Tassie collective dipole motion. In other words, the collective Tassie motion can significantly damps the current curls and divergencies initially produced by single-particle excitations. Instead, the CM and TM are not the Tassie modes and thus survive in the RPA case. The plots (c,d) show that CM determined by $\vec{\nabla} \cdot \vec{j}$ [see Eq. (9)] is concentrated at ∼25 MeV while TM determined by $\vec{\nabla} \times \vec{j}$ [see Eq. (8)] is distinctive at ∼7 MeV. Some $\vec{\nabla} \times \vec{j}$ strength still remains at 12–15 MeV.

In Fig. 8, the smoothed $E1(T = 0)$ form factors (35) for the values of interest are presented. Namely, the values $\vec{\nabla} \cdot \vec{j}$, $\vec{\nabla} \times \vec{j}$, j_+, and $\rho_0 \vec{\nabla} \times \vec{v}$ (pertinent for CM, TM, RW, and HD strengths) are considered. Unlike the above transition coordinate-energy maps, the form factors are direct constituents of (e,e') cross section and their inspection may suggest the most optimal transfer momenta k to observe desirable modes. As seen from Fig. 9, the observation of $\vec{\nabla} \cdot \vec{j}$ and $\vec{\nabla} \times \vec{j}$, and thus related CM (∼25 MeV) and TM (∼7 MeV), requests rather large momenta, $0.8\ \text{fm}^{-1} < k < 1.6\ \text{fm}^{-1}$, which testifies that CM and TM are mainly concentrated in the nuclear interior. Instead the form factors for j_+, and $\rho_0 \vec{\nabla} \times \vec{v}$ are maximal for lower momenta, $0.6\ \text{fm}^{-1} < k < 1.1\ \text{fm}^{-1}$, which points to their more surface character. Note that j_+ has strict maxima in both low-energy TM and high-energy CM regions. The form-factors for $\rho_0 \vec{\nabla} \times \vec{v}$ and $\vec{\nabla} \times \vec{j}$ are similar,

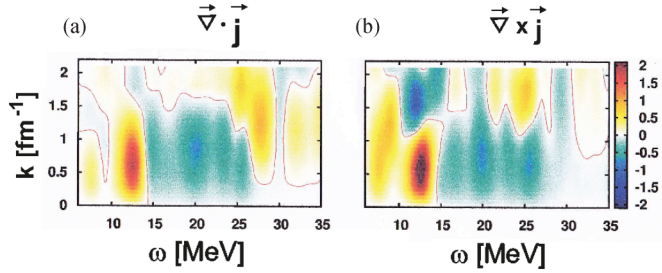

FIG. 9. (Color online) The $E1(T = 1)$ RPA formfactors (35) in ^{208}Pb for divergence (a) and curl (b) of the current. See explicit expressions for the patterns in Appendix B.

though the former is a bit stronger and shifted to lower k. The difference at low k arises because these two form factors are mainly distinguished by the coordinate dependence of the density $\rho_0(r)$, which is maximal at the nuclear surface (=low k).

For comparison, in Fig. 9, the isovector $E1(T = 1)$ RPA form factors for $\vec{\nabla} \cdot \vec{j}$ and $\vec{\nabla} \times \vec{j}$ are depicted. It is seen that they are weaker than in the $T = 0$ channel. The reason is again related to the dominant collective Tassie mode. Indeed, within the Goldhaber-Teller model [29], the GDR is essentially the Tassie mode. Hence we have the strong suppression of $\vec{\nabla} \cdot \vec{j}$ and $\vec{\nabla} \times \vec{j}$. Nevertheless, in Fig. 10, the GDR region still has noticeable $\vec{\nabla} \cdot \vec{j}$ and $\vec{\nabla} \times \vec{j}$ at 12–13 MeV. This signals that the actual GDR is a combination of the Goldhaber-Teller [29] (Tassie mode) and Steinwedel-Jensen [40] (beyond Tassie mode) flows. There are hints of the isovector TM at 11–13 MeV. The isovector CM is not seen. Perhaps it is shifted above the energy 35 MeV [as compared to the unperturbed 1ph CM strength at 29–35 MeV, depicted in Fig. 8(a)]. A comparison of Figs. 9 and 10 shows that the $T = 0$ channel is more suitable for the experimental search of TM and CM than the $T = 1$ one.

V. DISCUSSION

The strength functions, flow patterns, coordinate-energy maps, and form factors exhibited above show that j_+ component of the current has no any essential advantage over j_- as the vorticity indicator. Indeed both components: i) are peaked in TM (basically vortical) and CM (basically irrotational) regions, ii) have curls and divergences of the same order of magnitude in TM region. This indicates that j_+ or j_- alone cannot be a relevant measure of the vorticity. However, such a measure can be designed as a proper combination of j_+ or j_-. The toroidal mode is a natural case of such design. This transversal mode is free from the longitudinal part arising in the long-wave approximation (LWA) and its flow has a clear curl-like character.

As shown above, implementation of HD characteristics, like the velocity transition density $\delta\vec{v}$, is not convenient because of their unphysical behavior at the nuclear surface and beyond. To demonstrate the HD vorticity, it is better to use the toroidal flow which gives a similar vorticity and is well behaved near

the nuclear surface. Altogether, the numerical arguments favor TM as a measure of the vorticity.

For further discussion of nuclear vorticity, it is worth to define criteria for the *vortical* nuclear current. These could be: i) rotational flow pattern closely corresponding to the HD view, ii) decoupling from the CE i.e. transversal (divergence-free) character of the current. Such vortical nuclear current has to dominate in the TM which is mainly vortical and vanish in the CM whose flow pattern is mainly irrotational.

The above requirement ii) is closely related to the definition of the independent current component (ICC) [4,16] which, together with electric longitudinal (reduced to the nuclear density) and magnetic transversal components, should constitute a complete set describing the charge and current distributions in the nucleus. There are at least two ways to define ICC.

The first way to determine ICC is proposed by Heisenberg [16] and later Rawenthall and Wambach [4]. Here the decomposition of the current transition density

$$\delta\vec{j}(\vec{r}) = -i\sum_{\lambda\mu} a_{\lambda\mu}\,(j_{\lambda\lambda-1}(r)\,\vec{Y}^{*}_{\lambda\lambda-1\mu} + j_{\lambda\lambda+1}(r)\,\vec{Y}^{*}_{\lambda\lambda+1\mu}) \tag{36}$$

in terms of $j_- = j_{\lambda\lambda-1}(r)$ and $j_+ = j_{\lambda\lambda+1}(r)$ is used. The component j_+ is claimed CE-unrestricted despite the CE (2) actually couples the radial parts of $\delta\rho_\lambda$, j_-, and j_+:

$$\omega\delta\rho_\lambda(r) = -\sqrt{\frac{\lambda}{2\lambda+1}}\left(\frac{d}{dr} - \frac{\lambda-1}{r}\right) j_{\lambda\lambda-1}(r) + \sqrt{\frac{\lambda+1}{2\lambda+1}}\left(\frac{d}{dr} + \frac{\lambda+2}{r}\right) j_{\lambda\lambda+1}(r). \tag{37}$$

The claim is based on the analysis of the multipole moments given from the right and left sides of Eq. (37). The moments for $\delta\rho_\lambda$ and j_- are coupled,

$$\omega\int dr r^{\lambda+2}\delta\rho_\lambda(r) = \sqrt{\lambda(2\lambda+1)}\int dr r^{\lambda+1} j_{\lambda\lambda-1}(r), \tag{38}$$

while j_+ moments fully vanish. For this reason, j_+ is considered as CE-unrestricted and thus suitable to represent ICC and nuclear vorticity [4]. Following this prescription, the vorticity of the nuclear current is fully determined by its j_+ component.

By our opinion, this prescription is not good at least for the following reasons. First, the vanishing of j_+ moments decouples j_+ from CE only in the integral sense while preserving the local coupling (37). In other words, $\vec{\nabla}\cdot\vec{j}_+(\vec{r})$ is not locally zero. Indeed in Fig. 5(e) the field $\vec{\nabla}\cdot\vec{j}_+(\vec{r})$ is locally strong. However it has different sign at $z > 0$ and $z < 0$ and thus can vanish being integrated. Second, following Eq. (15), j_+ contributes to CM, which suggests a considerable vortical fraction in CM flow. At the same time, we know that CM is basically irrotational and has the gradient-like velocity [10]. Third, our numerical analysis of TM/CM strengths and curl/divergences of the current does not reveal any essential advantage of j_+ over j_- as the vorticity indicator. Altogether, the ansatz [4] to use j_+ as a measure of the vorticity and ICC looks doubtful.

Another (and more natural) way to define ICC has been proposed by Dubovik *et al.* [5]. Here the electric current transition density is decomposed into the longitudinal and transversal components,

$$\delta\vec{j}(\vec{r}) = \delta\vec{j}_{\parallel}(\vec{r}) + \delta\vec{j}_{\perp}(\vec{r}), \tag{39}$$

$$\delta\vec{j}_{\parallel}(\vec{r}) = \vec{\nabla}\phi(\vec{r}), \quad \delta\vec{j}_{\perp}(\vec{r}) = \vec{\nabla}\times\vec{\nabla}\times(\vec{r}\,\chi(\vec{r})), \tag{40}$$

where $\phi(\vec{r})$ and $\chi(\vec{r})$ are some scalar functions. As compared to the prescription [4,16], this way looks more logical for the search of CE-unrestricted divergence-free ICC. Now we get $\delta\vec{j}_\perp$ as the natural ICC candidate from very beginning.

The current components can be expanded in the basis of eigenfunctions $\vec{J}^{(\kappa)}_{\lambda\mu k}(\vec{r})$ ($\kappa = -, 0, +$) of the vector Helmholtz equation (the similar expansion is familiar for the vector-potential, see, e.g., [41]). Then the transversal component reads

$$\delta\vec{j}_{\perp}(\vec{r}) = \sum_{\lambda\mu k}\vec{J}^{(+)}_{\lambda\mu k}(\vec{r})\,m^{(+)}_{\lambda\mu}(k), \tag{41}$$

where $m^{(+)}_{\lambda\mu}(k)$ are electric transversal form factors and integration by k is assumed, In the LWA ($k \to 0$), the transversal component is reduced to the longitudinal one. After subtraction of the LWA part from $\delta\vec{j}_\perp$, we get at $k > 0$ the toroidal current density. The transversal character of the toroidal current is also seen from Eqs. (7) and (24). Being independent from $\delta\vec{j}_\parallel$ and thus decoupled from CE, the toroidal current can be considered both as ICC [5] and relevant vortical part of the complete nuclear current. Unlike the prescription [4,16], this vortical current is built from both j_+ and j_- components, see, e.g., (24). Its vorticity corresponds to HD one, see Sec. II C. Besides, the relevance of the TM current as a measure of the vorticity is confirmed by our numerical analysis of flow patterns. Altogether, our analysis shows that just TM and its current are best representatives of the nuclear vorticity.

Finally note that for more detailed study of the nuclear vorticity, it is desirable to go beyond RPA by taking into account the coupling to complex configurations, see, e.g., the relevant extensions [11,42–46]. Note that, for the proper treatment of anharmonic effects, inclusion only of two-phonon configurations may not be enough. The impact of higher configurations and exact record of the Pauli principle are also necessary, see discussion [46,47]. All these factors make anharmonic models very complicated. Anyway, before performing these involved investigations, a mere RPA exploration is desirable and this is just our case.

VI. CONCLUSIONS

The problem of nuclear vorticity in isoscalar $E1$ excitations (toroidal and compression modes—TM and CM) was scrutinized within the Skyrme RPA with the force SLy6. A representative set of characteristics (strength functions, flow pattern for currents and velocities, curls and divergences of the current and its components, coordinate-energy maps and form factors) was inspected. Analysis of curls $\vec{\nabla}\cdot\vec{j}$ and divergences $\vec{\nabla}\times\vec{j}$ of the nuclear current, as direct indicators of the vortical/irrotational flow and coupling to the

continuity equation (CE), was especially important. Note that the isovector GDR (within the Goldhaber-Teller model [29]) and isoscalar spurious c.m. motion, being the Tassie collective modes, have vanishing contributions to $\vec{\nabla}\cdot\vec{j}$ and $\vec{\nabla}\times\vec{j}$. Instead, the TM and CM do not belong the Tassie modes and for them the curls and divergences are indeed very instructive.

The numerical and analytical analysis shows that, unlike the prescription [4,16], the nuclear vorticity is better described not by j_+ component of the nuclear current but by its transversal toroidal part [5] composed from both j_+ and j_- components. The toroidal motion is well decoupled from the continuity equation, closely corresponds to the hydrodynamical picture of the vorticity, and provides a reasonable criterion of the vortical/irrotational flow in toroidal and compression modes in the $E1(T=0)$ channel.

ACKNOWLEDGMENTS

The work was partly supported by the GSI-F+E-2010-12, RE 322/14-1, Heisenberg-Landau (Germany - BLTP JINR), and Votruba- Blokhintsev (Czech Republic - BLTP JINR) grants. P.-G.R. is grateful for the BMBF support under Contracts No. 06 DD 9052D and 06 ER 9063. The support of the research plan MSM 0021620859 (Ministry of Education of the Czech Republic) and the grant of Czech Science Foundation (P203 – 13 – 07117S) are appreciated. We thank Prof. J. Wambach for useful discussions.

APPENDIX A: CURLS AND DIVERGENCIES

The curl and divergence of the current $E1$ transitions densities read

$$\vec{\nabla}\times\delta\vec{j}^{\nu}_{1}(\vec{r}) = i[\text{rot } j]^{\nu}(r)\,\vec{Y}^{*}_{11}, \tag{A1}$$

where

$$[\text{rot } j]^{\nu}(r) = \sqrt{\frac{2}{3}}\frac{d}{dr}j^{\nu}_{10}(r) + \sqrt{\frac{1}{3}}\left[\frac{d}{dr}+\frac{3}{r}\right]j^{\nu}_{12}(r) \tag{A2}$$

and

$$\vec{\nabla}\cdot\delta\vec{j}^{\nu}_{1\mu}(\vec{r}) = i[\text{div } j]^{\nu}(r)\,Y^{*}_{1}, \tag{A3}$$

where

$$[\text{div } j]^{\nu}(r) = \sqrt{\frac{1}{3}}\frac{d}{dr}j^{\nu}_{10}(r) - \sqrt{\frac{2}{3}}\left[\frac{d}{dr}+\frac{3}{r}\right]j^{\nu}_{12}(r). \tag{A4}$$

The velocity transition density can be decomposed like the current one (17):

$$\delta\vec{v}^{\nu}_{1\mu}(\vec{r}) = \left[v^{\nu}_{10}(r)\vec{Y}^{*}_{10\mu}(\hat{\vec{r}}) + v^{\nu}_{12}(r)\vec{Y}^{*}_{12\mu}(\hat{\vec{r}})\right], \tag{A5}$$

with

$$v^{\nu}_{10}(r) = \frac{j^{\nu}_{10}(r)}{\rho_0(r)}\,, \quad v^{\nu}_{11}(r) = \frac{j^{\nu}_{11}(r)}{\rho_0(r)}\,. \tag{A6}$$

Then

$$\vec{\nabla}\times\delta\vec{v}^{\nu}_{1\mu}(\vec{r}) = i[\text{rot } v]^{\nu}(r)\,\vec{Y}^{*}_{11}, \tag{A7}$$

$$\vec{\nabla}\cdot\delta\vec{v}^{\nu}_{1\mu}(\vec{r}) = [\text{div } v]^{\nu}(r)\,Y^{*}_{1} \tag{A8}$$

with

$$[\text{rot } v]^{\nu}(r) = \sqrt{\frac{2}{3}}\frac{d}{dr}v^{\nu}_{10}(r) + \sqrt{\frac{1}{3}}\left[\frac{d}{dr}+\frac{3}{r}\right]v^{\nu}_{12}(r), \tag{A9}$$

$$[\text{div } v]^{\nu}(r) = \sqrt{\frac{1}{3}}\frac{d}{dr}v^{\nu}_{10}(r) - \sqrt{\frac{2}{3}}\left[\frac{d}{dr}+\frac{3}{r}\right]v^{\nu}_{12}(r). \tag{A10}$$

APPENDIX B: INTEGRAL AND AVERAGE CHARACTERISTICS

The flows in Figs. 4–6 represent the integral vector variables (28) in $\{x, y=0, z\}$ cartesian plane, i.e., $\vec{A}(\vec{r}) = A_x(x, y=0, z)\vec{e}_x + A_z(x, y=0, z)\vec{e}_z$. In particular, variables (28) include

$$\vec{j} \to \vec{A}^{\nu}(\vec{r}) = \delta\vec{j}^{\nu}(\vec{r}), \tag{B1}$$

$$\vec{j}_{10} \to \vec{A}^{\nu}(\vec{r}) = j^{\nu}_{10}(r)\vec{Y}^{*}_{10}, \tag{B2}$$

$$\vec{j}_{12} \to \vec{A}^{\nu}(\vec{r}) = j^{\nu}_{12}(r)\vec{Y}^{*}_{12}, \tag{B3}$$

$$\vec{\nabla}\times\vec{j} \to \vec{A}^{\nu}(\vec{r}) = [\text{rot } j]^{\nu}(r)\vec{Y}^{*}_{11}, \tag{B4}$$

$$\vec{\nabla}\times\vec{j}_{10} \to \vec{A}^{\nu}(\vec{r}) = \sqrt{\frac{2}{3}}\frac{d}{dr}j^{\nu}_{10}(r)\vec{Y}_{11}, \tag{B5}$$

$$\vec{\nabla}\times\vec{j}_{12} \to \vec{A}^{\nu}(\vec{r}) = \sqrt{\frac{1}{3}}\left[\frac{d}{dr}+\frac{3}{r}\right]j^{\nu}_{12}(r)\vec{Y}^{*}_{11}, \tag{B6}$$

$$\vec{v} \to \vec{A}^{\nu}(\vec{r}) = \delta\vec{v}^{\nu}(\vec{r}), \tag{B7}$$

$$\rho_0(r)\vec{\nabla}\times\vec{v} \to \vec{A}^{\nu}(\vec{r}) = \rho_0(r)[\text{rot } v]^{\nu}(r)\vec{Y}^{*}_{11}. \tag{B8}$$

The values in Eqs. (B1)–(B3), (B4)–(B6), and (B7),(B8) are taken from expressions (17), (A1),(A2), and (A5)–(A7),(A9), respectively.

The scalar divergences in Figs. 4–6 involve the values

$$\vec{\nabla}\cdot\vec{j} \to B^{\nu}(\vec{r}) = [\text{div } j]^{\nu}(r)Y^{*}_{1}, \tag{B9}$$

$$\vec{\nabla}\cdot\vec{j}_{10} \to B^{\nu}(\vec{r}) = \sqrt{\frac{1}{3}}\frac{d}{dr}j^{\nu}_{10}(r)Y^{*}_{1}, \tag{B10}$$

$$\vec{\nabla}\cdot\vec{j}_{12} \to B^{\nu}(\vec{r}) = -\sqrt{\frac{2}{3}}\left[\frac{d}{dr}+\frac{3}{r}\right]j^{\nu}_{12}(r)Y^{*}_{1}, \tag{B11}$$

$$\rho_0(r)\vec{\nabla}\cdot\vec{v} \to B^{\nu}(\vec{r}) = \rho_0(r)[\text{div } v]^{\nu}(r)Y^{*}_{1} \tag{B12}$$

from expressions (A3),(A4) and (A8),(A6),(A10). The divergences are depicted in the figures as circles of the area proportional to $B(x, y=0, z)$. The filled (open) circles mean the positive (negative) variable.

Further, Figs. 7–9 give the average radial-energy maps (30) and form factors (35) using the values

$$\vec{\nabla}\times\vec{j} \to C^{\nu}(r) = [\text{rot } j]^{\nu}(r), \tag{B13}$$

$$\vec{\nabla}\cdot\vec{j} \to C^{\nu}(r) = [\text{div } j]^{\nu}(r) \tag{B14}$$

taken from expressions (A2) and (A4).

[1] A. Bohr and B. R. Mottelson, *Nuclear Structure*, Vol. 2 (Benjamin, New York, 1974).
[2] P. Ring and P. Schuck, *Nuclear Many Body Problem* (Springer-Verlag, New York, Heidelberg, Berlin, 1980).
[3] M. N. Harakeh and A. van der Woude, *Giant Resonances* (Clarendon Press, Oxford, 2001).
[4] D. G. Raventhall and J. Wambach, Nucl. Phys. A **475**, 468 (1987).
[5] V. M. Dubovik and A. A. Cheshkov, Sov. J. Part. Nucl. **5**, 318 (1975); V. M. Dubovik and L. A. Tosunyan, *ibid.* **14**, 504 (1983).
[6] S. F. Semenko, Sov. J. Nucl. Phys. **34**, 356 (1981).
[7] G. Holzwarth and G. Ekart, Z. Phys. A **283**, 219 (1977).
[8] G. Holzwarth and G. Ekart, Nucl. Phys. A **325**, 1 (1979).
[9] N. Paar, D. Vretenar, E. Khan, and G. Colo, Rep. Prog. Phys. **70**, 691 (2007).
[10] J. Kvasil, V. O. Nesterenko, W. Kleinig, P.-G. Reinhard, and P. Vesely, Phys. Rev. C **84**, 034303 (2011).
[11] N. Ryezayeva, T. Hartmann, Y. Kalmykov, H. Lenske, P. von Neumann-Cosel, V. Yu. Ponomarev, A. Richter, A. Shevchenko, S. Volz, and J. Wambach, Phys. Rev. Lett. **89**, 272502 (2002).
[12] A. Repko, P.-G. Reinhard, V. O. Nesterenko, and J. Kvasil, Phys. Rev. C **87**, 024305 (2013).
[13] F. E. Seer, T. S. Dumitrescu, T. Suzuki, and C. H. Dasso, Nucl. Phys. A **404**, 359 (1983).
[14] E. C. Caparelli and E. J. V. de Passos, J. Phys. G: Nucl. Part. Phys. **25**, 537 (1999).
[15] L. D. Landau and E. M. Lifshitz, *Course of Theoretical Physics: Hydrodynamics*, Vol. 6 (Butterworth-Heinemann, Oxford, 1987).
[16] J. Heisenberg, J. Lichtenstadt, C. N. Papanicolas, and J. S. McCarthy, Phys. Rev. C **25**, 2292 (1982).
[17] M. N. Harakeh, K. vanderBorg, T. Ishimatsu, H. P. Morsch, A. vanderWoude, and F. E. Bertrand, Phys. Rev. Lett. **38**, 676 (1977).
[18] S. Stringari, Phys. Lett. B **108**, 232 (1982).
[19] P.-G. Reinhard, Ann. Physik, **1**, 632 (1992).
[20] T. H. R. Skyrme, Phil. Mag. **1**, 1043 (1956).
[21] D. Vauterin and D. M. Brink, Phys. Rev. C **5**, 626 (1972).
[22] Y. M. Engel, D. M. Brink, K. Goeke, S. J. Krieger, and D. Vauterin, Nucl. Phys. A **249**, 215 (1975).
[23] M. Bender, P.-H. Heenen, and P.-G. Reinhard, Rev. Mod. Phys. **75**, 121 (2003).
[24] E. Chabanat, P. Bonche, P. Haensel, J. Meyer, and R. Schaeffer, Nucl. Phys. A **635**, 231 (1998).
[25] W. Kleinig, V. O. Nesterenko, J. Kvasil, P.-G. Reinhard, and P. Vesely, Phys. Rev. C **78**, 044313 (2008).
[26] V. O. Nesterenko, J. Kvasil, and P.-G. Reinhard, Phys. Rev. C **66**, 044307 (2002).
[27] V. O. Nesterenko, W. Kleinig, J. Kvasil, P. Vesely, P.-G. Reinhard, and D. S. Dolci, Phys. Rev. C **74**, 064306 (2006).
[28] L. J. Tassie, Austr. J. Phys. **9**, 407 (1956).
[29] M. Goldhaber and E. Teller, Phys. Rev. **74**, 1046 (1948).
[30] T. Suzuki and D. J. Row, Nucl. Phys. A **286**, 307 (1977).
[31] A. Bohr and B. R. Mottelson, *Nuclear Structure*, Vol. 1 (Benjamin, New York, 1969).
[32] J. Kvasil, N. Lo Iudice, Ch. Stoyanov, and P. Alexa, J. Phys. G: Nucl. Part. Phys. **29**, 753 (2003).
[33] D. A. Varshalovich, A. N. Moskalev, and V. K. Khersonskii, *Quantum Theory of Angular Momentum* (World Scientific, Singapore, 1976).
[34] A. V. Varlamov, V. V. Varlamov, D. S. Rudenko, and M. E. Stepanov, *Atlas of Giant Dipole Resonances* (IAEA, Vienna, 1999).
[35] M. Uchida *et al.*, Phys. Lett. B **557**, 12 (2003).
[36] M. Uchida *et al.*, Phys. Rev. C **69**, 051301(R) (2004).
[37] D. Vretenar, A. Wandelt, and P. Ring, Phys. Lett. B **487**, 334 (2000).
[38] D. Vretenar, N. Paar, P. Ring, and T. Niksic, Phys. Rev. C **65**, 021301(R) (2002).
[39] G. Colo, N. Van Giai, P. Bortignon, and M. R. Quaglia, Phys. Lett. B **485**, 362 (2000).
[40] H. Steinwedel and J. H. D. Jensen, Z. Naturforsch. A **5**, 413 (1950).
[41] J. M. Eisenberg and W. Greiner, *Excitation Mechanisms of the Nucleus: Electromagnetic and weak interaction* (North-Holland, Amsterdam, 1988).
[42] G. Colò and P. F. Bortignon, Nucl. Phys. A **696**, 427 (2001).
[43] A. P. Severyukhin, V. V. Voronov, and N. V. Giai, Phys. Rev. C **77**, 024322 (2008).
[44] E. Litvinova, P. Ring, and V. Tselyaev, Phys. Rev. C **78**, 014312 (2008).
[45] D. Bianco, F. Knapp, N. Lo Iudice, F. Andreozzi, and A. Porrino, Phys. Rev. C **85**, 014313 (2012).
[46] V. G. Soloviev, *Theory of Atomic Nuclei: Quasiparticles and Phonons* (Institute of Physics, Bristol, 1992).
[47] V. O. Nesterenko, Z. Phys. A - Atomic Nuclei **335**, 147 (1990).